Numerical investigation of a droplet impacting obliquely on a horizontal solid surface

Haibo Zhao,[1,4] Xing Han,[1] Jiayu Li,[2] Wei Li ⬤,[1] Tao Huang,[2] Peng Yu ⬤,[2,3,4,*] and Liqiu Wang[1,†]

[1]*Department of Mechanical Engineering, The University of Hong Kong, 999077 Hong Kong*

[2]*Department of Mechanics and Aerospace Engineering, Southern University of Science and Technology, Shenzhen 518055, China*

[3]*Guangdong Provincial Key Laboratory of Turbulence Research and Applications, Southern University of Science and Technology, Shenzhen 518055, China*

[4]*Center for Complex Flows and Soft Matter Research, Southern University of Science and Technology, Shenzhen 518055, China*

Obliquely impacting of droplet on horizontal solid surface is studied numerically. The impact velocity (v_1), both the magnitude and direction, is varied to analyze its effect on spreading area and droplet kinetics. The normal impact velocity (v_1^n) is found to be the main factor that influences the temporal variation of spreading area in droplet obliquely impacting process. The influence of normal Weber number (We_n) on the restitution coefficients (ε^n and ε^t) is also investigated. Within the same impact angle interval, the normal restitution coefficient (ε^n) grows with small We_n and is with the general scaling relationship of $\varepsilon^n \sim \mathrm{We}_n^{-1/4}$ for moderate We_n, which is similar to that in the droplet normal impact process. The tangential restitution coefficient (ε^t) is found to vary around a constant value and this observation has been analyzed from the view of both droplet kinetics and dynamics. Moreover, we also study the influence of tangential velocity on viscous dissipation and find that large tangential velocity would induce higher viscous dissipation energy.

I. INTRODUCTION

The impact of a droplet on solid surfaces is commonly encountered in nature and industry, including rain effect [1], inkjet printing [2], and spray cooling [3], and is thus of great academic and practical significance. Extensive works have focused on the normal impact in which the droplet velocity is perpendicular to the solid surface. When the splash limit is not exceeded, the droplet simply spreads over the surface until it reaches maximum radius. The spreading factor β, defined by the ratio of the maximum and initial radius, has attracted many researchers. Two dimensionless numbers are often employed to characterize this process, the Weber number (We) and the Reynolds number (Re), which are defined by $\mathrm{We} = \rho_l u_l^2 D_0/\sigma$ and $\mathrm{Re} = \rho u_l D_0/\mu_l$, where ρ_l, u_l, and μ_l are density, velocity, and dynamic viscosity of the droplet, respectively. D_0 is the initial droplet diameter, and σ is the surface tension coefficient. Based on the balance among the inertial, viscous, and capillary contributions, numerous relations between spreading factor and impact parameters have been established [4]. After spreading, depending on surface properties, the droplet could recede or remain close to the maximum spreading shape. When the surface is (super) hydrophobic, the

---

retraction could lead to partial or complete rebound. In this process, the contact time t_c, during which the drop stays in contact with the solid surface after impact, is another factor that arouses many researchers' interests. Besides, in some engineering application, the aim is to minimize t_c, like the anti-icing needs in the aviation field. It is found that the contact time only scales with the inertia-capillarity time τ when the droplet experiences the impact-spread-recoil-rebound phase on macroscopically flat superhydrophobic surfaces [5]. The inertia-capillarity time is defined by $\tau = \sqrt{\rho_l R_0^3 / \sigma}$, where R_0 is the initial radius. The scaling, $t_c / \tau = 2.2 \pm 0.3$, is notably irrespective of the droplet kinetic properties and holds in a certain range of Weber number. However, this scaling is not valid for other complex surfaces. For example, it is found that by adding a macrotexture as a ridge on the flat surface, the contact time reduces by approximately 37% [6]. In addition, a phenomenon called pancake bouncing [7] is also reported and it is demonstrated that this unconventional bouncing could reduce the contact time by a factor of 4. The physics behind the phenomenon has been widely studied [8,9].

During the droplet impact, the kinetic energy and surface energy would be exchanged and some of the energy would be consumed by the viscous dissipation. To characterize the energy loss after rebound, the restitution coefficient is defined by $\varepsilon = v_2 / v_1$, where v_1 is impact velocity and v_2 is rebound velocity. Thus, a higher Weber number would result in greater deformation and more dissipation. For droplets impacting normally on superhydrophobic carbon nanotube array, the restitution coefficient is proportional to $\mathrm{We}^{-1/4}$ at the range of $2 < \mathrm{We} < 100$ [10]. Aboud and Kietzig [11] also obtained similar results for the droplet impact on inclined superhydrophobic surfaces.

Droplet impact on the tilted surface has also been extensively studied since it displays some unique features different from the impact on horizontal surfaces, such as the back and front asymmetry deformation upon impingement. To specifically characterize the impact outcomes, the normal Weber number is defined by $\mathrm{We}_n = \rho_l (u_1 \cos \alpha_s)^2 D_0 / \sigma$, where α_s is the surface-inclined angle. Yeong *et al.* [12] demonstrated that at low We_n, droplet impacting on the horizontal and tilted surfaces behaved similarly. Nevertheless, at high We_n, the maximum spreading length is different due to the asymmetric motion of droplet and the asymmetry effects would become more pronounced as the inclination angle is increased. Due to inclination, the drop would slide tangentially across the solid surface. Thus, the slide length L is also a focus in the process. Through experiments, Aboud *et al.* [13] found that the increase of We_n would lead to a decrease in L/L_0, where L_0 is an idealized sliding length. This decreasing outcome is attributed to the drag forces acting on the droplet during the impact process. Yeong *et al.* [12] also reported that the surface inclination had no obvious effect on the contact time. By contrast, Antonini *et al.* [14] obtained the opposite conclusion that an increase in the inclination could promote the droplet rebound and shorten the contact time.

When the impact velocity increases to a critical value, splashing would occur and the threshold would change with the inclination angle [15]. In the normal impact, the splashing would occur when $\mathrm{We}\sqrt{\mathrm{Re}} > K$, where K is the splashing threshold. During the oblique impact process, the asymmetry impact could lead to an azimuthal variation of the ejected rim and thus a different splash threshold is derived. Bird *et al.* [16] have expanded the threshold for impact on horizontal surface to inclined surface by incorporating the lamella's spreading dynamics. Aboud *et al.* [15] proposed a linear model which includes the critical velocity for splashing at a normal angle of incidence and the tangential component of the impact velocity under the oblique circumstance. Both models agree well with the experiments.

When droplet impacts on flat or tilted surface, the impact velocity is aligned with gravity. However, in nature, the direction of the droplet motion is not always the same as gravity when other forces, such as wind, magnetic force, are involved. Thus, the droplet would obliquely impact the surface. Sun *et al.* [17] examined the oblique impact of droplets on microstructured superhydrophobic surfaces and identified four possible types of bouncing. Schremb *et al.* [18] studied the influence of temperature on the oblique droplet impact process. Zhu *et al.* [19] reported the nonspecular reflection of droplet impingement onto solid surfaces with a dimple and utilized this phenomenon to

enable versatile droplet manipulation. So far, the work concerning the droplet obliquely impinging on horizontal surface is limited. There are many phenomena and mechanisms deserving further investigation, such as the influence of the reflection process on the droplet morphology and kinetics, how the impact angle affects energy exchange, and so on. In the present study, we will address and investigate these questions using the numerical method. The rest of the paper is organized as follows: the numerical method is described and validated in Sec. II. In Sec. III, the outcomes of the droplet obliquely impacting on solid horizontal surface are presented. The velocity, both the magnitude and direction, would be varied to study their effects on droplet deformation and kinetics, including the droplet spreading area, tangential velocity of the mass center, and restitution coefficients. The energy transfer is also studied. Finally, the concluding remarks are drawn in Sec. IV.

II. DESCRIPTION OF THE NUMERICAL METHOD

A. Governing equation and discretization

In multiphase flow simulation, various methods are employed to track the interface evolution explicitly or implicitly, such as the front track [20], level set [21], and volume of fluid [22] methods. Among these methods, the volume of fluid (VOF) is widely used due to its simpler implementation and mass-preservation merits. In the VOF method, an indicator function called phase fraction, α, is introduced and commonly defined as

$$\alpha = \begin{cases} 0 & \text{if the cell is occupied by air} \\ 0 < \alpha < 1 & \text{if the cell contains both air and liquid.} \\ 1 & \text{if the cell is occupied by liquid} \end{cases} \tag{1}$$

And, the governing equation for α is

$$\frac{\partial \alpha}{\partial t} + \nabla \cdot (\alpha \vec{u}) = 0, \tag{2}$$

where $\vec{u}$ is the velocity vector.

The governing equations are, for two-phase immiscible and incompressible flow,

$$\nabla \cdot \vec{u} = 0, \tag{3}$$

$$\frac{\partial (\rho \vec{u})}{\partial t} + \nabla \cdot (\rho \vec{u} \vec{u}) = -\nabla p + \nabla \mu [\nabla \vec{u} + (\nabla \vec{u})^T] + \rho \vec{g} + \vec{F}, \tag{4}$$

where p is the pressure, μ is the dynamic viscosity, ρ is density, $\vec{g}$ is the gravity acceleration, and $\vec{F}$ accounts for the surface tension.

In the present simulation, the two immiscible fluids in each cell are considered as a single medium with the physical properties calculated as the weighted averages based on the local value of the volume fraction functions and the constitution properties. The volume-fraction averaged density and viscosity in each cell are given as follows:

$$\rho = \alpha \rho_l + (1 - \alpha) \rho_g, \tag{5}$$

$$\mu = \alpha \mu_l + (1 - \alpha) \mu_g, \tag{6}$$

where ρ_l, ρ_g and μ_l, μ_g are densities and dynamic viscosities of liquid and air, respectively. It could be seen that the physical properties vary in cells that are cut by the interface.

In the present study, the interFoam solver on the OPENFOAM platform is used to perform all simulations. To constrain the interface diffusion in the simulation, Eq. (3) is modified as

$$\frac{\partial \alpha}{\partial t} + \nabla \cdot (\vec{u} \alpha) + \nabla \cdot (\vec{u}_r \alpha (1 - \alpha)) = 0, \tag{7}$$

where $\vec{u}_r = \vec{u}_l - \vec{u}_g$ is the relative velocity between the two fluids. $\vec{u}_r$ is evaluated at each computation cell,

$$\vec{u}_r = (\min(C_{\alpha i}|\vec{u}|, \max(|\vec{u}|)))\frac{\nabla \alpha_i}{\left|\nabla \alpha_i\right|}, \tag{8}$$

where $C_{\alpha i}$ is the compression coefficient, which determines the degree of compression. In the present study, $C_{\alpha i}$ is equal to unity in all simulation cases. To keep the volume fraction field bounded, Eq. (7) is solved by using the MULSE (Multidimensional Universal Limiter with Explicit Solution) method, which is based on the method of flux-corrected transport [23,24].

In the interFoam solver, the effect of surface tension is considered by adding a source term $\vec{F}$ in the momentum equation. The surface tension force is evaluated according to the continuum surface force model developed by Brackbill *et al.* [25], which reads

$$\vec{F} = \sigma\kappa\nabla\alpha, \tag{9}$$

where κ is the mean curvature and evaluated as

$$\kappa = -\nabla \cdot \vec{n}. \tag{10}$$

In Eq. (10), $\vec{n}$ is the unit vector normal to the interface and far from the wall, which is defined as

$$\vec{n} = \nabla\alpha \ / \ |\nabla\alpha|. \tag{11}$$

At the solid surface, the unit vector $\vec{n}$ is modified by the contact angle [26].

In OPENFOAM, the finite-volume method is employed to discretize the governing equations, which subdivides the computational domain into discrete nonoverlapping elements. The variables are located at the center of these elements. Due to the incompressibility of the flow, pressure and velocity are coupled implicitly. PIMPLE algorithm is adopted to solve Eqs. (3) and (4) simultaneously in the interFoam solver, which combines PISO (Pressure Implicit Split Operator) and SIMPLE (Semi-Implicit Method for Pressure-Linked Equations) algorithms and allows the usage of a larger time step [27].

B. Dynamic contact angle model

The contact angle θ_0 is commonly adopted to characterize the wettability of a surface by a specific liquid, which is defined as the angle enclosed by the tangent to the liquid-gas and the solid-liquid interface at the three-phase sessile contact line. For the ideal surface under equilibrium conditions, θ_0 can be calculated by using Young's equation if the surface energy density of each of the phase interfaces is known. However, in most practical cases, the surfaces are not ideally smooth, for which the contact angle hysteresis phenomenon should be considered. This means that the contact angle varies over a certain range. The upper and lower limits of this range are known as the advancing contact angle (θ_a) and the receding contact angle (θ_r). Thus, in this study, a dynamical contact angle model called the Kistler model [28] is implemented in the interFoam to predict the droplet impacting phenomenon. The Kistler model is commonly used and has been verified in many previous studies [29,30]. In the model, the contact angle depends on the contact line velocity and can be evaluated through the following expressions:

$$\theta_{dyn} = \begin{cases} f_{Hoff}\big[\mathrm{Ca} + f_{Hoff}^{-1}(\theta_a)\big] & \text{if Ca} > 0 \\ \theta_0 & \text{if Ca} > 0, \\ f_{Hoff}\big[\mathrm{Ca} + f_{Hoff}^{-1}(\theta_r)\big] & \text{if Ca} > 0 \end{cases} \tag{12}$$

where f_{Hoff} is Hoffman function and is defined as follows:

$$f(x) = \arccos\left\{1 - 2\tanh\left[5.16\left(\frac{x}{1 + 1.31x^{0.99}}\right)^{0.706}\right]\right\}, \tag{13}$$
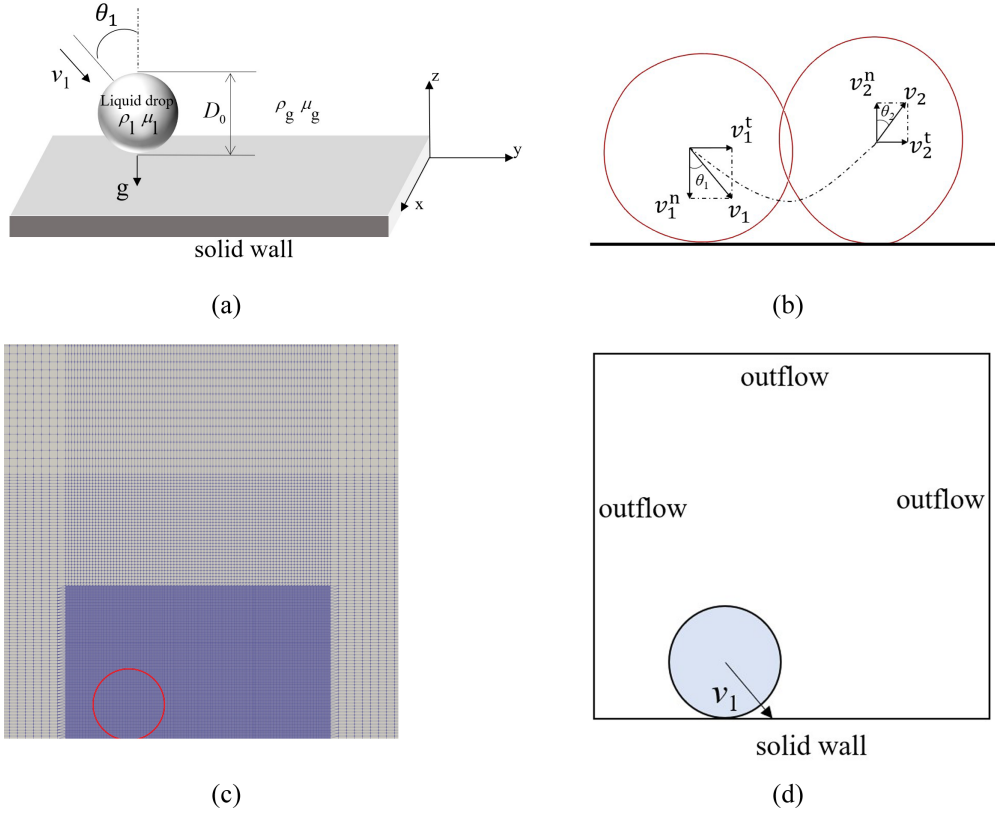
FIG. 1. Schematic sketch of simulation. (a) Droplet obliquely impacts on the horizontal solid wall. D_0 is the initial diameter of the droplet. v_1 is the impact velocity with the impact angle θ_1. (b) Droplet impacts on and rebounds from the solid surface. v_1^n and v_1^t are the normal and tangential components of the impact velocity. v_2^n and v_2^t are the normal and tangential components of the rebound velocity. θ_1 is the impact angle and θ_2 is the rebound angle. (c) Mesh used for the numerical simulation; the inner part enclosing the motion behavior is refined. The red circle denotes the initial droplet. (d) The boundary conditions imposed on the computational domain.

and f_{Hoff}^{-1} is the inverse function of Hoffman function, Ca is the capillary number and is defined as

$$\mathrm{Ca} = \frac{\mu_1 V_{\mathrm{cl}}}{\sigma}, \tag{14}$$

where V_{cl} is the contact line velocity and is calculated as the relative velocity between the solid wall and the neighboring cell next to it.

C. Geometry and simulation parameters

The setup of the three-dimensional simulation is sketched in Fig. 1(a). Consider a liquid drop with a diameter D_0, density ρ_1, and dynamic viscosity μ_1, impacting on solid surface at an angle θ and a speed v_1. The surrounding gas has density ρ_g and dynamic viscosity μ_g. The liquid-gas surface tension coefficient is σ. The material physical properties are listed in Table I.

TABLE I. Material physical properties.

Physical material	Value
Liquid density ρ_l	$997.05 \, \text{kg m}^{-3}$
Gas density ρ_g	$1.185 \, \text{kg m}^{-3}$
Liquid kinematic viscosity v_l	$0.89 \times 10^{-6} \, \text{m}^2 \, \text{s}^{-1}$
Gas kinematic viscosity v_g	$1.549 \times 10^{-5} \, \text{m}^2 \, \text{s}^{-1}$
Surface tension coefficient σ	$0.072 \, \text{N m}^{-1}$

The droplet is initially placed on a solid surface without air beneath it. The initial velocity field is assigned by

$$\vec{u}_0 = \begin{cases} 0 & \text{if } \alpha = 0 \\ v_1(\sin\theta\vec{j} - \cos\theta\vec{k}) & \text{if } \alpha = 0 \end{cases}. \tag{15}$$

The diameter of the droplet is fixed with $D_0 = 2 \, \text{mm}$. The normal and tangential components of the impact velocity v_1^n and v_1^t, as shown in Fig. 1(b), are varied to study the influence on droplet dynamics. All simulations are run on the computational domain of $5D_0 \times 5D_0 \times 5D_0$. To save the grid resources, the grid is only refined in the part enclosing the motion behavior before the start of the simulation, as shown in Fig. 1(c). The no-slip boundary condition is imposed for solid wall and the outflow condition is imposed on other boundaries, as shown in Fig. 1(d).

D. Validation

The simulation of droplet impacting on the superhydrophobic substrate is performed to test the accuracy of the present numerical approach with the experiment data. In the the experiment, the impact process is monitored with a high-speed camera (Phantom M110). The impacting drop is released from a needle which is connected with a pump. The superhydrophobic surface is coated with silanized silica nanoparticles using commercialized Glaco (Soft99) and the postbaking is performed. The impact velocity is $0.3 \, \text{m} \, \text{s}^{-1}$, and the corresponding Weber number is equal to 2.5. Figure 2 shows the comparison of the experimental and numerical results. It is observed that the numerical droplet profile agrees well with the experiment.

Four meshes with different grid sizes are used to test the grid independence. The grid size is listed in Table II. It is noted that these grid sizes would only be employed in the region where the mesh is refined.
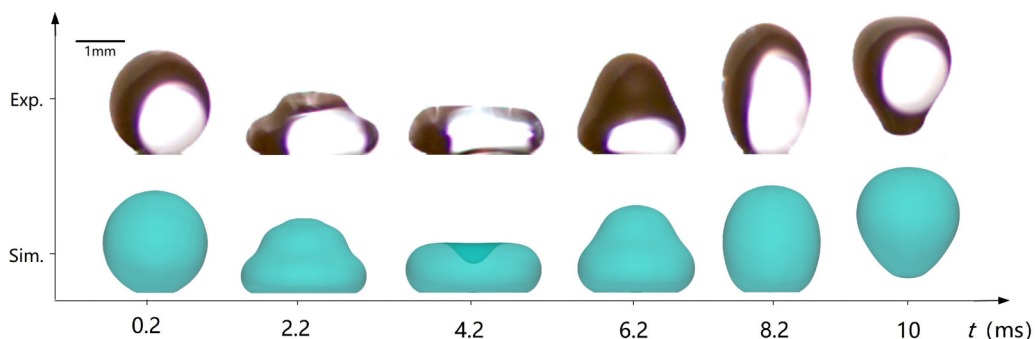

FIG. 2. Comparison of experimental (top) and numerical (bottom) results for droplet normal impact on solid surface. Droplet diameter equals 2.0 mm and the impact velocity is $0.3 \, \text{m} \, \text{s}^{-1}$. The equilibrium, advancing, and receding contact angles have the same value of 155°. Scale bar: 1 mm.

TABLE II. Four meshes with different grid size.

Simulation tests	Grid size in the refined part
Case 1	$220 \times 220 \times 220$
Case 2	$300 \times 300 \times 300$
Case 3	$330 \times 330 \times 330$
Case 4	$360 \times 360 \times 360$

In Fig. 3(a), the dimensionless spreading diameter $D^* = D/D_0$ is plotted as a function of dimensionless time $t^* = t/\tau$ for different simulation cases and the experiment results. Good agreement exists between the experiment data and the numerical results and the characteristic transition states are accurately captured. For example, at around $t^*_{max} = 0.87$, the droplet reaches the maximum diameter (the experiment result $D^*_{max} = 1.0$ and the numerical result $D^*_{max} = 1.1$). After t^*_{max}, the droplet begins shrinking. At around $t^* = 1.62$, the shrinking rate decreases to nearly zero and the spreading diameter keeps fixed for around 0.23 dimensionless time. After $t^* = 1.85$, the droplet shrinks again until the droplet detaches from the rigid surface at $t^* = 2.6$. These typical moments predicted in our simulations are well consistent with those observed in the experiment. The slight difference between the predicted and experiment diameters may be attributed to the measurement error and the condition discrepancy between the simulation and experiment environment.

A mesh independence study is also analyzed. The relative error (RE) caused by the mesh size can be written as

$$\mathrm{RE} = \frac{\left| D_i^{max} - D_4^{max} \right|}{D_4^{max}} \times 100\%,$$ (16)

where D_i^{max} is the maximum diameter in the ith case ($i = 1, 2, 3$). Figure 3(b) shows the relative error versus the mesh resolution. It is concluded that when the grid size is smaller than that of the second case, the relative error is below 1% and the resolution of the mesh has negligible influence on the simulation results. Therefore, in the following study, the mesh resolution in the second case is employed.

To further validate the simulation results, the maximum drop-spreading factor ξ_{max} ($\xi_{max} = D_{max}/D_0$) is also analyzed and compared with the theoretical models. Different theoretical models
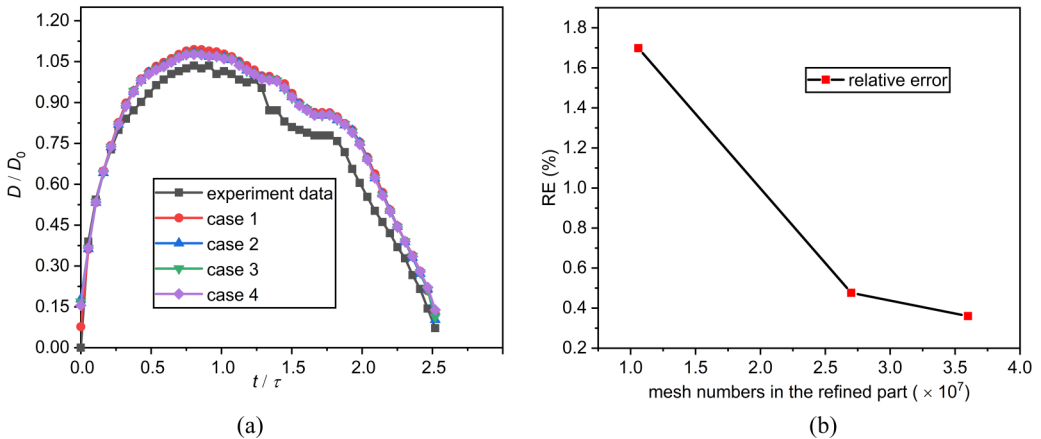

(a)   (b)

FIG. 3. (a) Comparison of simulation and experiment results: the normalized spreading diameter (D/D_0) vs the dimensionless time (t/τ); (b) the relative error vs the mesh resolution.
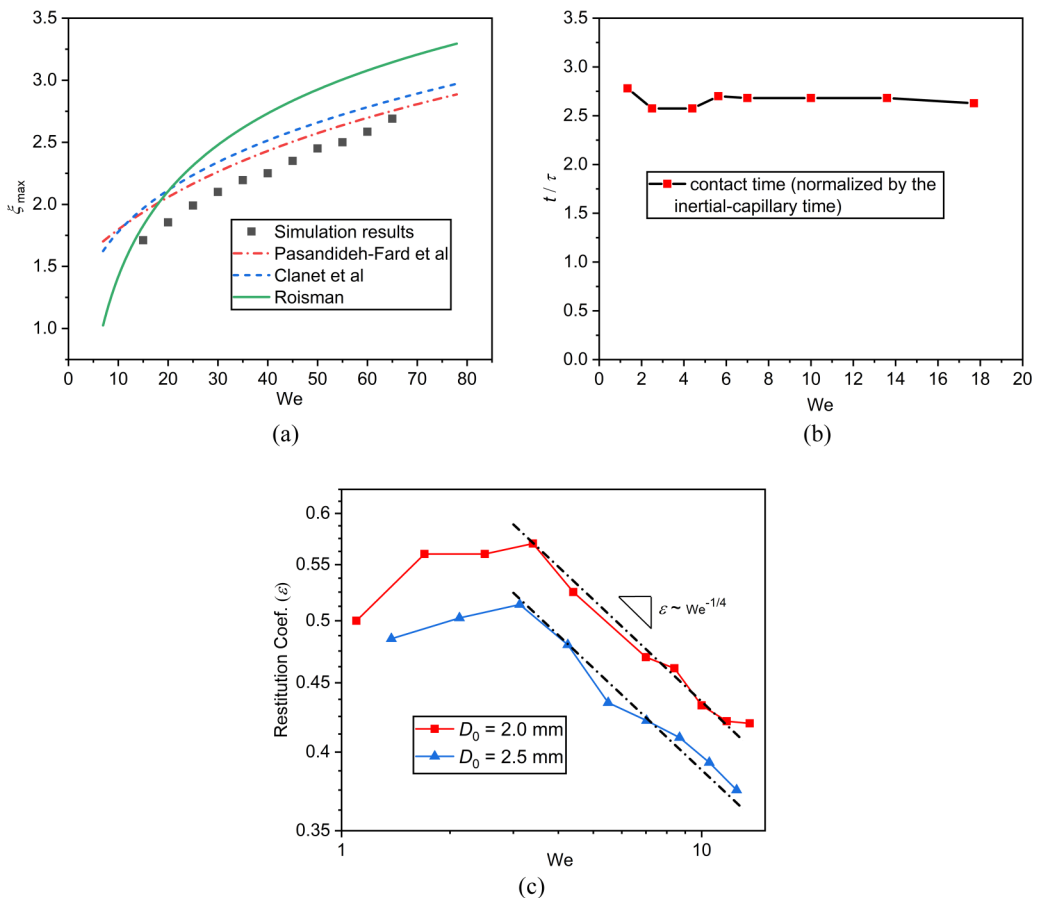
FIG. 4. Droplet normal impact on a hydrophobic surface. (a) Comparison of the numerically predicted maximum spreading factor (ξ_{max}) with the droplet diameter of 2.0 mm. The present simulation results (black square) are compared to the models of Pasandideh-Fard *et al.* [31] (red line), Clanet *et al.* [32] (green line), and Roisman [33] (blue line). (b) Numerically predicted spreading time with different We. (c) The simulation of the restitution coefficient with different We (red square and blue triangle).

have been proposed in the literature. Pasandideh-Fard *et al.* [31] proposed that the expression of ξ_{max} is predicted as: $\xi_{max} \sim \sqrt{\frac{We+12}{3(1-\cos\theta_a)+4WeRe^{-1/2}}}$, where θ_a is the advancing contact angle. In the model of Clanet *et al.* [32], the spreading factor is calculated in another form $\xi_{max} \sim We^{1/4}$. The third theoretical prediction is derived by Roisman [33] and its form is $\xi_{max} \sim 0.87Re^{1/5} - 0.4Re^{2/5}We^{-1/2}$. Figure 4(a) plots the maximum spreading factor versus Weber number. The range of the Weber number is $15 \sim 65$ and is achieved by varying the impact velocity. It is observed that the models of Pasandideh-Fard *et al.* [31] and Clanet *et al.* [32] display similar results with a maximum difference only up to 4.56%. The simulation result is close to the two models and bears a stronger agreement with Pasandideh-Fard *et al.* [31]. Pasandideh-Fard *et al.*'s model [31] considered the effects of the Weber and Reynolds numbers as well as the contact angle. Note that the contact angle has great effects on the maximum spreading area [34], which, however, is not included in Clanet *et al.*'s and Roisman *et al.*'s models. This could explain the relatively larger discrepancies between the present simulation and these two models.

Pasandideh-Fard *et al.* [31] compared the model with the experiment results and found that when the Reynolds number is higher, the model agrees well with the experiment results. However, when

the Reynolds number is lower, the discrepancies become larger. This is because the assumption of a thin boundary layer is no longer valid at lower Reynolds number. This tendency also agrees well with our simulation result, as indicated in Fig. 4(a).

The contact time t_c is also predicted and analyzed using numerical simulations. It has been mentioned that t_c is independent of impact velocity and satisfies the scaling $t_c \sim \beta\tau$, where τ is the inertial-capillarity time. Thus, for a constant-diameter droplet impacting at varying velocity, t_c is expected to stay unchanged. Figure 4(b) plots the simulation results of the relationship between t_c/τ and We. In all the cases, the diameter of the droplet maintains constant. As expected, the contact time is independent of the impact velocity, which is proportional to τ with the coefficient β being about 2.7.

Moreover, the restitution coefficient is analyzed to validate the simulation results. The rebound velocity v_2 is calculated as

$$v_2 = \frac{\sum_i m_i u_i}{M}, \tag{17}$$

where m_i and u_i are the mass and velocity of the liquid in one computational element on the rebound, respectively, and M is the total mass of the liquid. The Weber number is within the range of $1.1 < $ We < 11.74, during which the droplet is kept intact and no breakup occurs. The simulation results are plotted in Fig. 4(c). The simulation is performed with two droplet sizes ($D_0 = 2.0$ and 2.5 mm) and each size has the similar trend with We.

In the low range of We, the restitution coefficient increases with We. When the droplet impacts on the solid surface, a boundary layer forms near the solid surface and the boundary layer thickness δ is inversely proportional to $\sqrt{\text{Re}}$ [31]. Thus, smaller velocity would lead to larger δ. The viscous dissipation mainly occurs within the boundary layer. Since the viscous dissipation function ϕ can be estimated as $\phi \sim \mu(\frac{V_1}{\delta})^2$, ϕ would be negligible for smaller impact velocity. The energy conservation equation (before and after impact) could be simplified as $E_k^1 + E_s^1 = E_k^2 + E_s^2$, where E_k and E_s are the kinetic and surface energy and the superscripts 1 and 2 represent the impact and detach moment, respectively. This equation could be modified into $\frac{E_k^2}{E_k^1} = 1 - \frac{E_s^2 - E_s^1}{E_k^1}$. In addition, small We would result in slight surface area difference before and after impact and $E_s^2 - E_s^1$ could be assumed constant. Thus, $\frac{E_k^2}{E_k^1}$ ($= \varepsilon^2$) increases with E_k^1 ($= \frac{1}{2}Mv_1^2$) for small We, which indicates that ε increases with We within the low range of We. Within the moderate range of We, the viscous dissipation energy dominates the surface energy and the restitution coefficient ε would decrease with We. This decline agrees with the experiment results [10,11,35] that ε and We has the correlation $\varepsilon \sim \text{We}^{-1/4}$. It is noted that in our simulation that the droplet size has an influence on the correlation coefficient. Thus, it is reasonably assumed that the restitution coefficient may not only depend on We but also some other parameters that include droplet diameter. This needs further study and is out of the scope of the present study.

Note that the spurious interfacial currents commonly exist in two-phase simulation, especially when the density ratio between the two phases is large. Herein, the spurious currents are discussed in detail under the present occasion. Figure 5 plots the velocity magnitude $|u|$ contour for the droplet normal impact velocity of 0.3 m s^{-1}. We focus on the upper right part of the droplet, which is circled by the yellow square. At the time $t = 0.4$ and 1.4 ms, this part should be still undisturbed and maintain the initial velocity of 0.3 m s^{-1}. Thus, the occurrence of the spurious interfacial currents can be easily detected in this part if $|u|$ significantly deviates from 0.3 m s^{-1}. Since the air and liquid phases are continuous and there is no slip on the interface, the velocities of air and liquid phases near the interface in the yellow square box should have the same value. However, the variation in the velocity magnitude in this part does indicate that the spurious interfacial currents occur around the interface and are distributed nonuniformly. Four particular points (P_1 to P_4) are marked in the regions with the spurious interfacial currents in the right panel of Fig. 5(a). The corresponding velocity magnitudes of these four points are denoted by U_1, U_2, U_3, and U_4, respectively. Note that these four points are located in the air phase, with the values of $U_1 = 0.515$ m s^{-1}, $U_2 = 0.184$ m s^{-1},
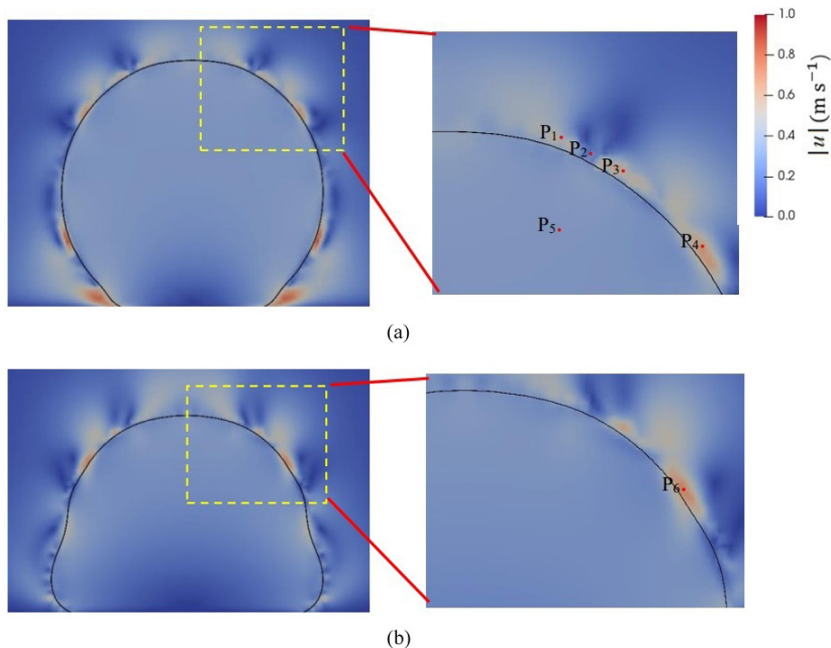
FIG. 5. The snapshots of droplet normal impacting on a solid surface at (a) $t = 0.4$ ms and (b) $t = 1.4$ ms. The yellow dashed square box in each left panel is enlarged in the corresponding right panel. The initial impact velocity is 0.3 m s^{-1}.

$U_3 = 0.598$ m s^{-1}, and $U_4 = 0.67$ m s^{-1}. For comparison, a point (P_5) is also marked in the water phase, with the corresponding velocity magnitude $U_5 = 0.3$ m s^{-1}. It demonstrates that the spurious interfacial currents oscillate around 0.3 m s^{-1}, with the overshoots U_1, U_3, U_4, and the undershoot U_2. It can be concluded that the velocity of the spurious interfacial current is of the same order of magnitude as the real one. Figure 5(b) plots the $|u|$ contour at $t = 1.4$ ms. The point P_6 in the region with the spurious interfacial currents has the velocity magnitude of $U_6 = 0.69$ m s^{-1}, which is also of the same order of magnitude as the initial impact velocity. It should be emphasized that the spurious interfacial currents mainly exist in the air phase [24]. In addition, the gas density is much smaller than the liquid one. These two features can minimize the adverse effects of the spurious interfacial currents.

The above agreement between the simulation results and the experiments or theoretical predictions confirms the validity of our numerical simulation for analyzing droplet obliquely impacting on horizontal solid surface.

III. RESULTS

A. Droplet obliquely impacting on horizontal surface

In this section, droplet obliquely impacting on horizontal solid surface is simulated. The problem has been described in Figs. 1(a) and 1(d). In the simulation, two sizes of droplet would be used, $D_0 = 2.0$ and 2.5 mm. v_1^n varies from 0.2 to 0.6 m s^{-1} and v_1^t from 0.1 to 0.5 m s^{-1}, yielding the range of We from 1.38 to 21.18, which is sufficiently small to keep the droplet intact. Figure 6 shows obliquely impacting process ($v_1^n = 0.5$ m s^{-1}, $v_1^t = 0.5$ m s^{-1}). Figure 6(a) is the side view of the process. The arrows indicate the flow direction and the color represents the magnitude of the velocity. It could be observed that the entire process also experiences an impact-spreading-retraction-rebounding process. However, due to the presence of v_1^t, the droplet would bounce
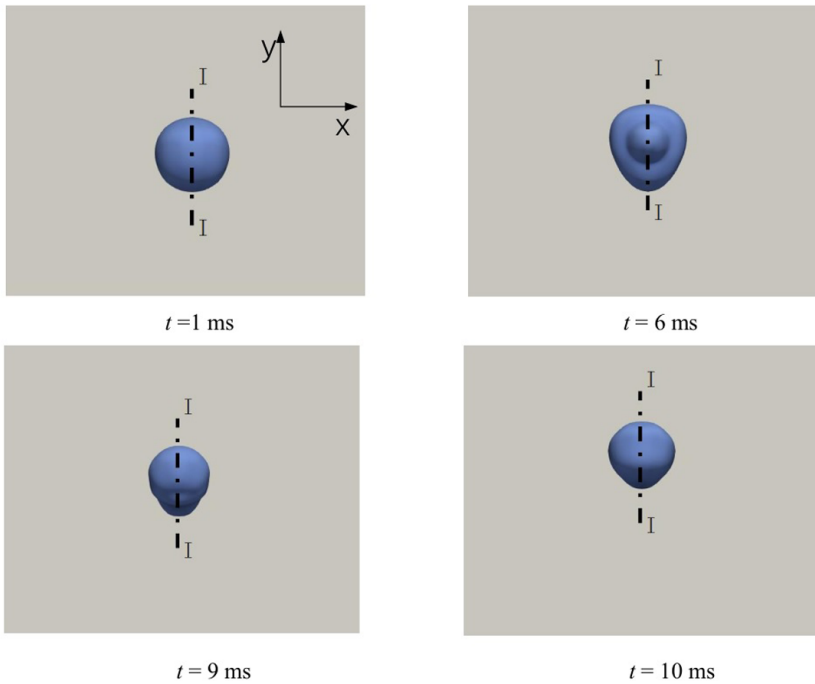
(a) side view
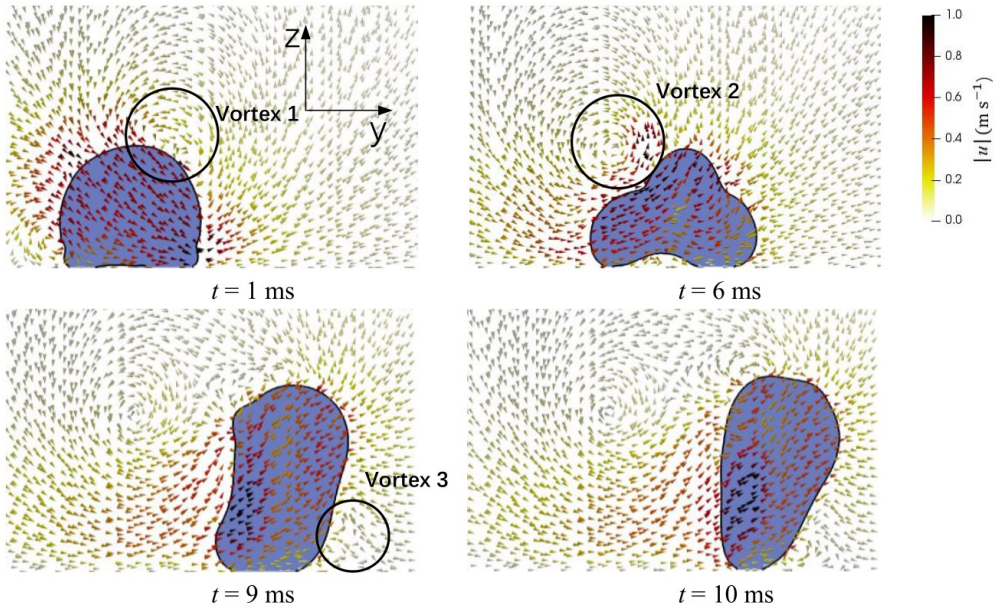
(b) top view

FIG. 6. Exemplary time sequence of droplet obliquely impacting solid surface ($v_1^n = 0.5$ m s^{-1}, $v_1^t = 0.5$ m s^{-1}). (a) Side view of the droplet motion. It can be observed that the droplet experiences an impact-spreading-retraction-rebounding process and would bounce asymmetrically on the y-z plane due to the presence of v_1^t; (b) Top view of the droplet motion. The projection of droplet surface on the x-y plane is noncircular and the trajectory of the droplet centroid is in the same plane (I-I) in the entire motion process.
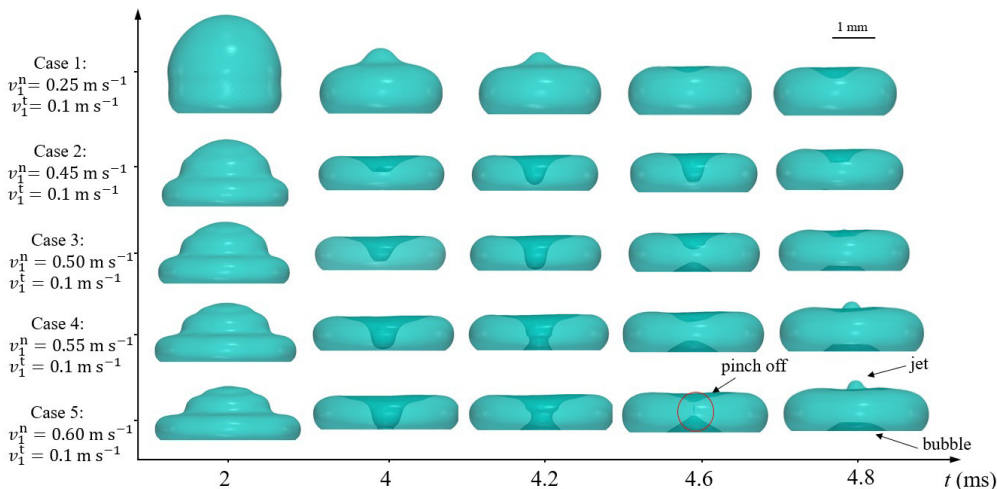
FIG. 7. Instantaneous isosurfaces with $\alpha = 0.5$ for five cases. Case 1: $v_1^n = 0.25$ m s^{-1}, $v_1^t = 0.1$ m s^{-1}; case 2: $v_1^n = 0.45$ m s^{-1}, $v_1^t = 0.1$ m s^{-1}; case 3: $v_1^n = 0.50$ m s^{-1}, $v_1^t = 0.1$ m s^{-1}; case 4: $v_1^n = 0.55$ m s^{-1}, $v_1^t = 0.1$ m s^{-1}; case 5: $v_1^n = 0.60$ m s^{-1}, $v_1^t = 0.1$ m s^{-1}; an air cavity with cylinder shape is formed in cases 2, 3, 4, and 5 and the air cavity would reach the solid surface only in cases 3, 4, and 5.

asymmetrically on the y-z plane. The asymmetry would influence the flow structure in ambient air and the drop itself. For example, due to the relative motion between the droplet and air, air vortices occur along the droplet surface (as labeled vortex 1, vortex 2, and vortex 3). These vortices are so small that they have little influence on the droplet motion.

From the top view in Fig. 6(b), the projection of droplet surface on the x-y plane is not fully circular while sliding on the surface due to the existence of v_1^t. In addition, the droplet keeps symmetrical on the x-z plane and v_1^t has a little influence on the x position of the droplet centroid. Thus, the trajectory of the droplet centroid is in the same plane (I-I) in the entire motion process.

Figure 7 plots the translucent isosurfaces with $\alpha = 0.5$ for five cases with the corresponding v_1^n of 0.25, 0.45, 0.50, 0.55, and 0.60 ms^{-1}, respectively. v_1^t is fixed at 0.1 ms^{-1} for all five cases. It is observed that a capillary wave generates at the bottom of the droplet when the droplet initially contacts the solid surface. This wave would propagate along the droplet surface and deform the droplet into conical shape. As the droplet continues spreading, the wave would travel to the droplet surface center and form a cylindrical air cavity if the magnitude of impact velocity v_1^n is sufficiently large (e.g., cases 2, 3, 4, and 5) [34–37]. As v_1^n increases, the air cavity would reach the solid surface (e.g., cases 3, 4, and 5) and the contact area between the droplet and the solid surface reduces. In the retraction stage, the air cavity would also shrink. The top of the cavity would retract faster than the bottom because the bottom of the cavity would be retarded by the viscous force near the surface. Due to the faster recoil rate and the narrower diameter at the middle part of the cavity, a pinch-off would occur at this position. As a result, the pinch-off would leave a bubble entrapped on the solid surface and a liquid jet emitted upward. In the later stage of the rebounding, the bubble would be released into the air.

Due to the noncircular contact area, the diameter is not appropriate to reflect the interaction between the droplet and the solid surface. Thus, temporal variation of spreading area (S) is investigated. Figure 8 demonstrates the relationship between the normalized spreading area $S^* = S/S_0$ (S_0 is the surface of the initial droplet) and the normalized time $t^* = t/t_c$. In Fig. 8(a), v_1^t and the droplet diameter are kept fixed ($v_1^t = 0.1$ m s^{-1}, $D_0 = 2.0$ mm), and v_1^n varies from 0.35 to 0.60 m s^{-1}. It could be figured out that the $t^* \sim S^*$ curve is different with v_1^t. In the spreading phase, S^* grows with t^* and the cases with larger v_1^n have higher growth rates. Similarly, when
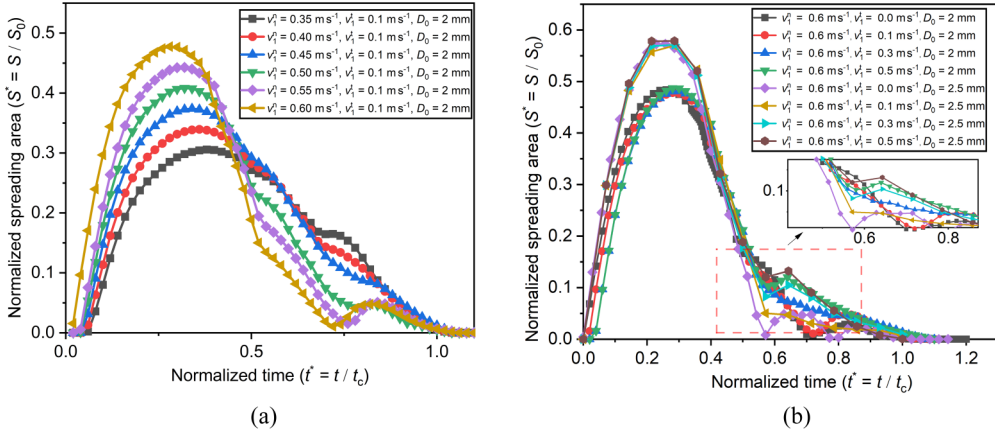
FIG. 8. Temporal variation of normalized droplet spreading area S^*. (a) v_1^t and droplet diameter is fixed. v_1^n varies from 0.35 to 0.60 m s^{-1}. In the spreading phase, S^* grows and the rate increases with v_1^n. Instead, in the retraction phase, S^* declines faster with larger v_1^n; (b) v_1^n is 0.60 m s^{-1}. For the same droplet size, S^* has similar behavior over the normalized time t^*, irrespective of v_1^t. The inset shows that there is a spike on the $t^* \sim S^*$ curve, which is due to the disappearance of the air cavity.

the droplet begins retracting, S^* starts falling and the cases with larger v_1^n fall faster. This faster decline could be attributed to the occurrence of the cylindrical air cavity, which emerges for larger v_1^n. Figure 8(b) plots the temporal variation of the normalized droplet spreading area S^* for the cases with the same v_1^n but different v_1^t. The results indicate that the cases with the same droplet size have a similar $t^* \sim S^*$ relationship, irrespective of v_1^t. Thus, it could be concluded that v_1^n is the main factor that influences the temporal variation of spreading area during the oblique impact process for the droplet of the same size.

It is noticed that there is a spike on the $t^* \sim S^*$ curve as indicated by the zoomed-in area in Fig. 8(b). Therefore, the spreading area would experience an increasing period in the retraction phase, which is due to the disappearance of the air cavity shown in Fig. 7. Figure 9 plots the velocity fields and phase distributions when the droplet is about to leave the surface. In the later stage, the left part of the droplet would firstly detach from the surface, as indicated by the red arrow in Fig. 9(a). The air would be expelled out from the bottom of the droplet surface due to the inertial force imposed by the adjacent liquid phase, which is marked in the yellow circle in Figs. 9(a) and 9(b). Thus, the part of the droplet separated by the air would contact the solid surface, which enlarges the spreading area.

Another interesting observation is the temporal variation of the tangential part of the mass center velocity v_t. Figure 10 plots the normalized tangential velocity ($v_t^* = v_t/v_1^t$) versus the normalized time ($t^* = t/t_c$). It is found that v_t^* decreases linearly with t^*. It is noted that the slope k is equal to $(at_c)/v_1^t$, where a is the effective acceleration when the droplet moves on the solid surface. Figure 10(a) plots the cases with a constant v_1^t. It could be observed that the normalized tangential velocity of the same droplet diameter lies on the same fitting line (fitting line 1 and fitting line 2). The slope is -0.285 and -0.312, respectively. Figure 10(b) plots the $t^* \sim v_t^*$ curves for the cases with the same v_1^n for each droplet size, which shows that the rate of decline is slightly different for each v_1^t and the average slope of the fitting lines is about -0.285. The mechanism behind this phenomenon involves the interplay between the interfacial deformation of the impacting droplet and the forces acting on the droplet, which will be analyzed qualitatively in Sec. III B.

B. Restitution coefficient

From the energy standpoint, the droplet impacting and rebounding are characterized by the exchange of kinetic and surface energy. In this process, some energy would be consumed by the
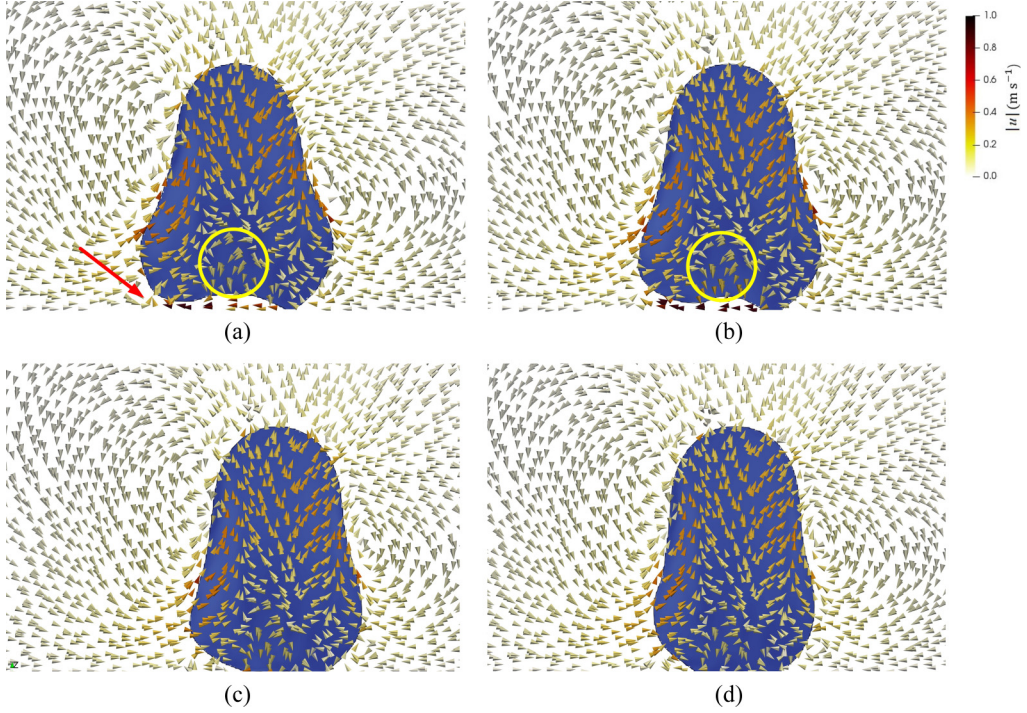
FIG. 9. The later stage for the droplet detaching from the solid surface. It could be observed that the left part of the droplet leaves the solid surface firstly and the air would be expelled out from the bottom of the droplet surface due to the inertial force imposed by the adjacent liquid phase. (a) $t^* = 0.74$ ms; (b) $t^* = 0.76$ ms; (c) $t^* = 0.78$ ms; and (d) $t^* = 0.80$ ms.

viscous losses or transferred into modes of vibration in the rebounded droplet. Due to the net loss in energy, the velocity of the rebounded droplet (v_2) is always less than its initial velocity (v_1). Thus, the restitution coefficient, defined as the ratio of v_2 and v_1, is always used to represent the loss
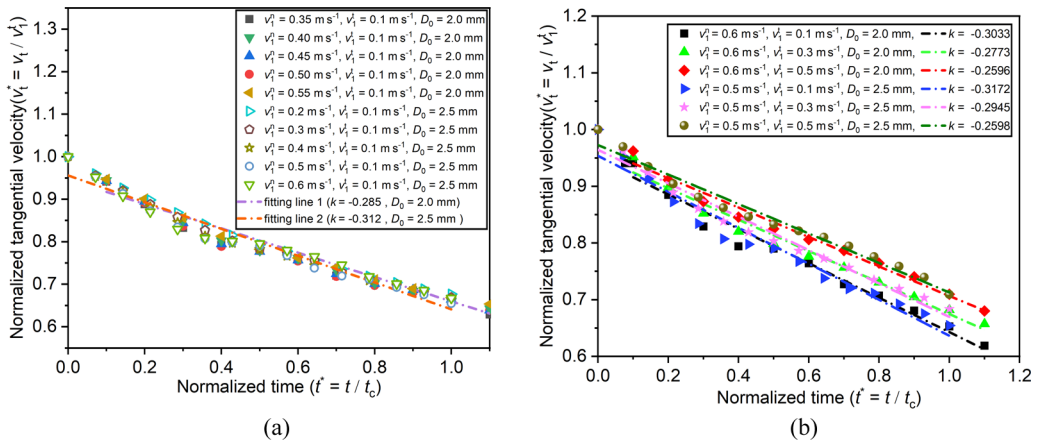

FIG. 10. Temporal variation of v_t. The solid symbols represent the cases with $D_0 = 2.0$ mm and the hollow ones represent the cases with $D_0 = 2.5$ mm. The dashed lines are the fitting lines. (a) v_1^t is kept constant at 0.1 m s^{-1}, and v_1^n and the droplet size are varied; (b) for each droplet size, v_1^n is kept constant at 0.6 m s^{-1} and v_1^t is varied.
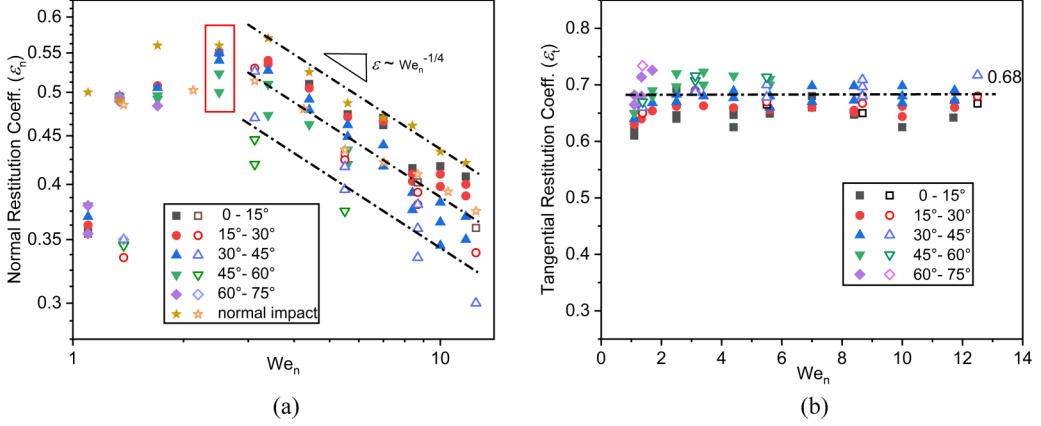
FIG. 11. Droplets obliquely impact on the horizontal solid surface. The solid symbols represent the cases with $D_0 = 2.0$ mm and the hollow ones represent $D_0 = 2.5$ mm. (a) $We_n \sim \varepsilon^n$ relationship. The star represents the normal impact and other symbols represent the obliquely impacting with different impact angle θ_1. (b) $We_n \sim$ 'ε^t relationship. ε^t scatters around 0.68 for all cases.

of energy. For convenience and clearness, two restitution coefficients are defined in this study, the normal restitution coefficient ε^n and the tangential restitution coefficient ε^t:

$$\varepsilon^n = v_2^n/v_1^n , \quad \varepsilon^t = v_2^t/v_1^t, \tag{18}$$

where v_1^n and v_1^t are the normal and tangential components of the impact velocity, and v_2^n and v_2^t are the normal and tangential components of the rebound velocity, as shown in Fig. 1(b).

1. Normal restitution coefficient

Similar to the normal droplet impact, the relation between We_n and ε^n is plotted in Fig. 11(a). The star indicates droplet normal impacting on solid surface. The solid symbols represent the cases with $D_0 = 2.0$ mm and the hollow ones represent the cases with $D_0 = 2.5$ mm. Depending on the impacting angle, all simulation cases could be categorized into five groups and every group has an interval of 15°. It could be observed that in the low range of We_n, ε^n increases with We_n, like that in the droplet normal impact. For moderate We_n, ε^n decreases and the relationship $\varepsilon^n \sim We_n^{-1/4}$ still works approximately for each interval. Regarding the cases with the same We_n, ε^n declines with the impacting angle θ_1, as shown in the cases encircled by the red box in Fig. 11(a). It is noted that v_1^t increases with the impact angle θ_1. Thus, it could be inferred that v_1^t would change the energy transfer among the kinetic energy, surface energy, and viscosity dissipation energy, which will be analyzed in Sec. III C.

2. Tangential restitution coefficient

The relationship between ε^t and We_n is plotted in Fig. 11(b). It is observed that ε^t scatters around 0.68. In fact, this value is related to the slope of the $t* \sim v_t^*$ curve in Sec. III B. Accordingly, in the period that the droplet is contact with the solid surface, the tangential velocity decreases linearly with the time:

$$\frac{v_1^t - v_2^t}{t_c} = a, \tag{19}$$

where a is the effective acceleration. According to the definition of tangential restitution coefficient, Eq. (19) could be modified into

$$\varepsilon^t = 1 + \frac{at_c}{v_1^t} = 1 + k, \tag{20}$$

where k is exactly the slope of the $t^* \sim v_t^*$ curve. The average of k is about -0.285 and consequently ε^t approximates 0.715, which agrees well with the above observation.

The variation of tangential coefficient with We_n could also be qualitatively analyzed from a dynamical view. Considering a droplet with constant size and a small Re, the shear force and the tangential velocity follow the relationship $F_s \sim v_t$ [38] in the whole sliding process. Thus, the average shear force could be expressed as $\vec{F_s} = k\vec{v_t}$, where k is assumed to be a constant coefficient. In addition, the tangential component of the velocity v_t is assumed to be linear within the contact period. With this assumption, $\vec{F_s}$ could be modified as

$$\vec{F}_s = k\left(\frac{v_1^t + v_2^t}{2}\right). \tag{21}$$

By applying the impulse theorem $\vec{F_s}\,\Delta t = M(v_1^t - v_2^t)$, where Δt equals contact time t_c and has nothing to do with the velocity, and M is the droplet mass, Eq. (21) can be rewritten as

$$\varepsilon^t = \frac{v_2^t}{v_1^t} = \frac{M/t_c - k/2}{M/t_c + k/2}. \tag{22}$$

Equation (22) indicates that the tangential restitution coefficient only depends on M, t_c, and k, which are assumed to be constant for the same droplet size. Thus, for the droplet with the constant size, ε^t would be fixed irrespective of the initial velocity.

3. Relation of $\theta_1 \sim \theta_2$

The reflection of droplet could enable versatile droplet manipulation, e.g., trapping, shedding, and on-demand coalescence of droplets [19]. This manipulation demands a better understanding of the traits of droplet reflection. Droplet reflection is analogous to light reflection, which obeys the reflection law. In this part, we examine whether droplet reflection within the present parameter range satisfies the laws [19]: (i) the incident droplet, the reflected droplet, and the surface normal lie in the same plane, (ii) the incident angle θ_1 is equal to the reflected (rebound) angle θ_2, and (iii) the reflected droplet and the incident droplet are on the opposite sides of the normal. The first and the third laws are satisfied according to the observation in Sec. III A. However, during oblique impact, the droplet reflection would deviate from specular reflection because the tangential velocity of the droplet is decelerated when the drop is sliding on the solid surface. The detailed relationship between $\theta_1 \sim \theta_2$ is investigated in this section.

Based on the definition of restitution coefficients and Fig. 1(b), the relationship $\theta_1 \sim \theta_2$ is written as

$$\theta_2 = \arctan\left(\frac{v_2^t}{v_2^n}\right) = \arctan\left(\frac{\varepsilon^t}{\varepsilon^n} \cdot \frac{v_1^t}{v_2^n}\right) = \arctan\left(\frac{\varepsilon^t}{\varepsilon^n} \cdot \tan(\theta_1)\right) \tag{23}$$

Equation (23) shows that the $\theta_1 \sim \theta_2$ relationship is dependent on the ratio of ε^t and ε^n. When the ratio is larger than unity, the rebound angle is larger than the impact angle and vice versa. For convenience, Figure 12 plots the $\theta_1 \sim \theta_2$ relation at different normal impact velocities with $D_0 = 2.0\,\text{mm}$. The black arrow indicates the direction along which We_n increases. The black dashed-dotted line is a reference line with the slope equal to unity. It could be observed that θ_2 is approximately linear with θ_1 and the slope depends on We_n. To clarify the impact of We_n on the slope of $\theta_1 \sim \theta_2$ curve, the relation is split into two figures, Figs. 12(a) and 12(b). In Fig. 12(a), We_n is within the range of $1.1 \sim 2.5$, where the slope decreases with We_n. In Fig. 12(b), We_n is within the range of $2.5 \sim 11.74$ and the slope increases with We_n.

Equation (23) implies that the $\varepsilon^t \sim We_n$ and $\varepsilon^n \sim We_n$ relationships are the main factors behind the above opposite trend. These two relationships have been analyzed in Secs. II D and III B 2. ε^t scatters around a constant value for all considered We_n because the shear force is linearly proportional to the tangential velocity for small Re. ε^n increases with We_n within the low range
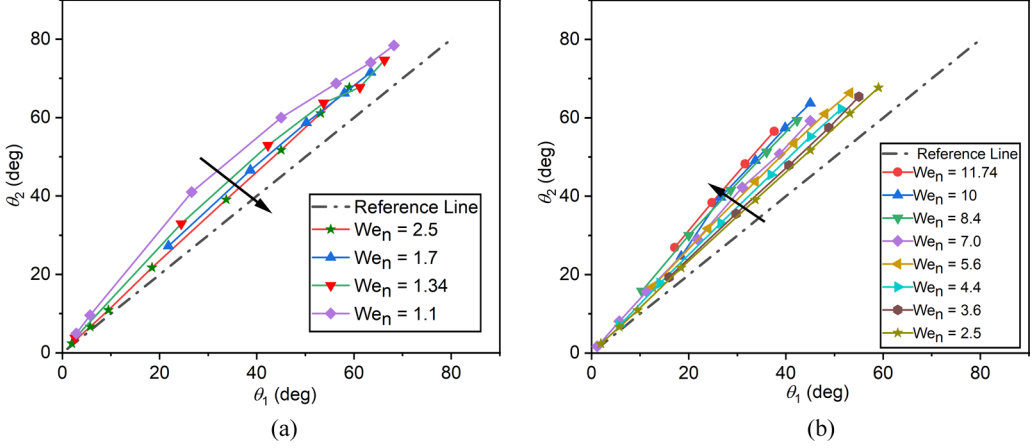
FIG. 12. Relationship between θ_2 and θ_1. (a) The range of We_n is $1.1 \sim 2.5$. The slope of $\theta_1 \sim \theta_2$ curve declines with We_n. (b) The range of We_n is $2.5 \sim 11.74$. The slope of $\theta_1 \sim \theta_2$ curve increases with We_n. The black arrow indicates the direction along which We_n increases. The dashed-dotted line is a reference line with the slope equal to unity.

of We_n owing to the small amount of viscous dissipation. As a result, the ratio $\varepsilon^t/\varepsilon^n$ decreases with We_n within the low range of We_n. Within the moderate range of We_n, ε^n declines due to larger viscous dissipation and the ratio $\varepsilon^t/\varepsilon^n$ increases with We_n. This opposite trend between $\varepsilon^t/\varepsilon^n$ and We_n has an impact on the slope of $\theta_1 \sim \theta_2$ according to Eq. (23). As a result, between $We_n = 1.1$ and 2.5 the behavior converges towards specular reflection while above $We_n = 2.5$ the trend is inverse. This opposite trend results from the competition between the shear stress induced by the tangential velocity v_l^t and the viscous force developed in the boundary layer during the droplet spreading and retracting processes.

Figure 11 demonstrates that within the considered range of We_n, the tangential restitution coefficient ε^t is larger than the normal restitution coefficient ε^n. Thus, the ratio between ε^t and ε^n is larger than unity. With Eq. (23), it could be inferred that θ_2 is larger than θ_1, which is expected in Figs. 12(a) and 12(b). It concludes that the second droplet reflection law is violated. However, this violation could offer the opportunity to navigate the droplet even more freely [19].

C. Energy analysis

In this section, the influences of v_l^t on the temporal variation of surface energy (SE), kinetic energy (KE), and viscous dissipation energy (VDE) is investigated. The gravity potential energy is negligible due to the small size of the droplet. KE is calculated as $\oint 0.5\rho_l v^2 d\Omega$ and SE is equal to σS, where Ω is the droplet volume and S is the liquid interface area. The energy by viscous dissipation is defined as

$$\text{VDE} = \int_0^t \int_0^\Omega \phi d\Omega dt, \qquad (24)$$

where ϕ is the viscous dissipation function and calculated as

$$\phi = \mu \left[2\left(\frac{\partial u_x}{\partial x}\right)^2 + 2\left(\frac{\partial u_y}{\partial y}\right)^2 + 2\left(\frac{\partial u_z}{\partial z}\right)^2 + \left(\frac{\partial u_x}{\partial y} + \frac{\partial u_y}{\partial x}\right)^2 + \left(\frac{\partial u_y}{\partial z} + \frac{\partial u_z}{\partial y}\right)^2 + \left(\frac{\partial u_z}{\partial x} + \frac{\partial u_x}{\partial z}\right)^2 \right], \qquad (25)$$

where u_x, u_y, and u_z are the x, y, and z components of the liquid velocity u, respectively.

Figure 13(a) plots the time evolution of the normalized kinetic energy [$KE^* = KE/KE_0$, where KE_0 is equal to $\oint 0.5\rho_l(v_l^n)^2 d\Omega$], the normalized surface energy ($SE^* = SE/SE_0$, where SE_0 is
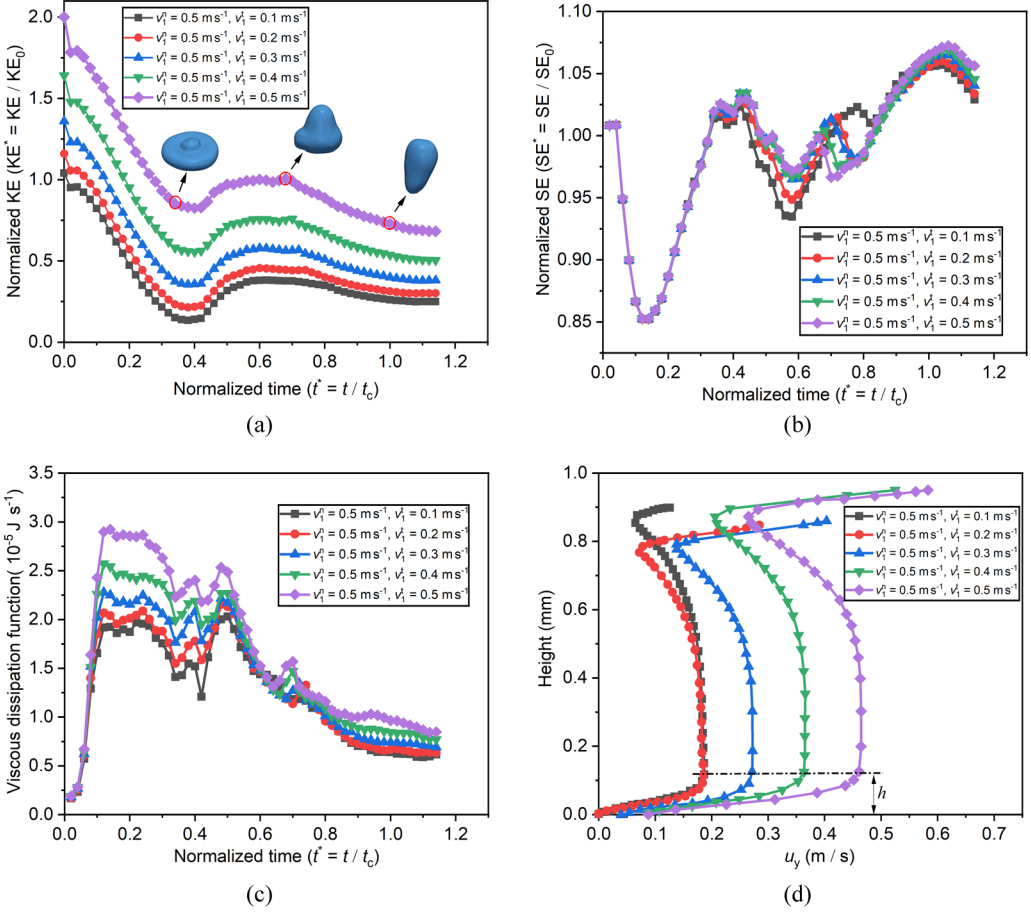
FIG. 13. Time evolution of (a) the normalized kinetic energy, (b) the normalized surface energy, and (c) viscous dissipation function within the droplet during the period that the droplet is contact with the solid surface. (d) the y component of the liquid velocity along the central line of the droplet at $t^* = 0.3$. The droplet initial diameter D_0 is 2.0 mm.

the initial droplet surface energy and calculated as the initial droplet surface area times the surface tension coefficient), and the viscous dissipation function integrated within the droplet. The droplet initial diameter D_0 equals 2.0 mm. In the early stage ($t^* = 0 \sim 0.1$), due to the sudden velocity change of the droplet in the surface vicinity, the viscous dissipation function rises rapidly, which results in the decline of KE* and SE*. With the spreading of the droplet, KE* continues to decrease and the reduction energy transfers into SE* and VDE. It is also figured out that at the same moment ($t^* = 0.4$), all the cases reach the maximum spreading area. After spreading, the retraction occurs and it would return part of SE* into KE* and consequently cause the rise of KE* ($t^* = 0.4 \sim 0.6$). During the time $t^* = 0.6 \sim 1.0$, KE* would keep decreasing due to the growth of SE* and the energy dissipated by the viscosity. In this period, it is noted that there are valleys on the $t^* \sim$ SE* curves as shown in Fig. 13(b). It is partially contributed to the disappearance of the air cavity, as explained in Sec. III A. When the air cavity disappears, a small part of the air-water interface would contact the solid surface, which induces the decline of droplet surface area and SE*.

In Fig. 13(c), it could be observed that larger v_1^t would intensify the viscous dissipation function at the spreading stage. This conclusion could be solidified by Fig. 13(d), which plots the y component of liquid velocity (u_y) in the droplet along the central line at $t^* = 0.3$. It could be observed that
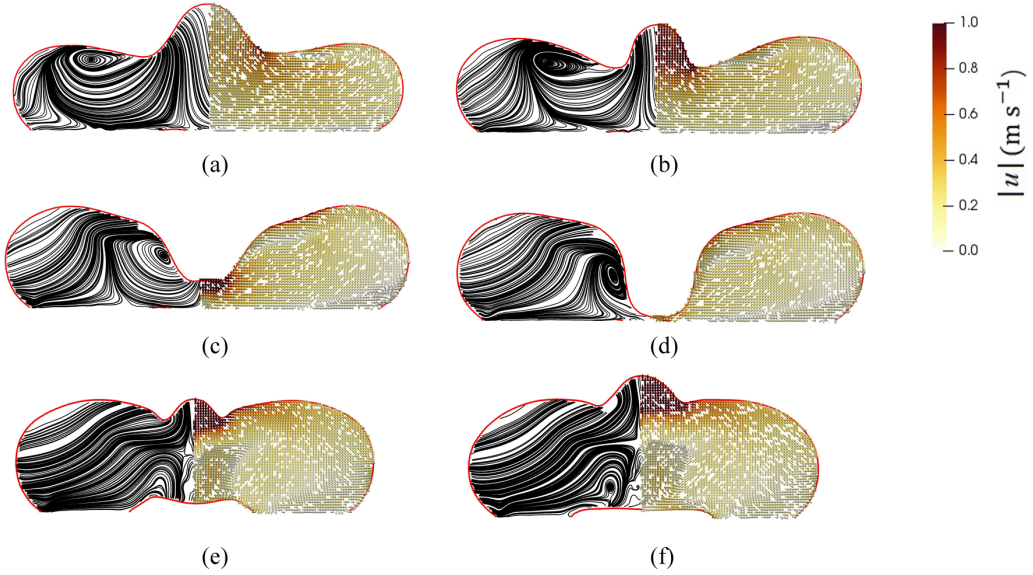
FIG. 14. The streamlines (left) and velocity field (right) for the oblique impact case ($v_1^n = 0.5$ m s^{-1}, $v_1^t = 0.1$ m s^{-1}) at different instantaneous time: (a) $t^* = 0.32$, (b) $t^* = 0.36$, (c) $t^* = 0.4$, (d) $t^* = 0.42$, (e) $t^* = 0.48$, and (f) $t^* = 0.5$.

near the solid surface the ratio $\Delta u_y / \Delta h$ grows with v_1^t. According to Eq. (23), this growth would intensify the viscous dissipation function and consequently more kinetic energy could be dissipated by viscous force. Thus, it could explain the observation in Sec. III B 1 that for the same v_1^n, larger v_1^t would cause more VDE and consequently smaller v_2^n, which results in the smaller normal restitution coefficient.

To further examine the temporal change of the viscous dissipation, Fig. 14 plots the streamlines (left part) and the velocity field (right part) at different instantaneous times for the oblique impact case with $v_1^n = 0.5$ m s^{-1} and $v_1^t = 0.1$ m s^{-1}. It could be observed that the vortex flow exists due to the competition between the surface tension force and the inertial force. At the spreading stage, the flow would spread radially due to the inertial force. However, the surface tension force, which has the tendency to minimize the surface area, would inhibit the flow. Afterwards, a vortex would develop beneath the upper surface of the droplet and build up until the droplet reaches the maximum spreading area (around $t^* = 0.4$). In the spreading stage, the cylindrical air cavity is formed and the vortex exists just beneath the upper surface of the droplet. When the cylindrical air cavity becomes pronounced ($t^* = 0.36$, 0.4, and 0.42), the vortex would move with the flow and along the surface from the droplet periphery to the center and eventually be trapped near the bottom surface. In the above process, flow circulation always exists within the droplet, which accounts for all above-zero viscous dissipation function values and the plateau between $t^* = 0.2 \sim 0.6$ in Fig. 13(c).

IV. CONCLUDING REMARKS

Obliquely impacting of the droplet on horizontal flat solid surface is investigated numerically with interFoam solver in this study. The impact velocity is varied, both its direction and magnitude, to study its influence on droplet spreading area and the restitution coefficients.

By analyzing the relationship $t^* \sim S^*$, it is observed that the normal velocity is the main factor that influences the spreading area, irrespective of the tangential velocity and the droplet size. Another observation about droplet kinetics is that the relationship $t^* \sim v_t^*$ is linear and the slope is slightly different for all cases.

The restitution coefficient is decomposed into the normal restitution coefficient ε^n and the tangential restitution coefficient ε^t. Within the same impact angle interval, ε^n grows with small We_n and the general scaling relationship of $\varepsilon^n \sim We_n^{-1/4}$ holds in the moderate range of We_n. For the same v_1^n, larger v_1^t leads to higher viscous dissipation and more kinetic energy is transferred into internal energy. Therefore, for the same v_1^n, larger v_1^t results in smaller ε^n. Within the range of We_n investigated in the present study, it is also found that ε^t changes slightly and varies around 0.68 in all cases, independent of We_n and θ_1. This phenomenon is analyzed from kinetic and dynamic view and is related to the slope of $t^* \sim v_t^*$ relationship.

The relation of $\theta_1 \sim \theta_2$ is also analyzed. For the same We_n, θ_2 is linear with θ_1. Due to the different monotonicity of ε^t and ε^n, the influences of We_n on the slope of the $\theta_1 \sim \theta_2$ curve could be divided into two ranges. Over the low range of We_n, the slope decreases with We_n. Over the moderate range of We_n, the slope grows with We_n. In addition, because the ratio between ε^t and ε^n is larger than unity, θ_2 is always larger than θ_1.

In the energy analysis of droplet obliquely impacting, it is found that near the solid surface the ratio $\Delta u_y / \Delta h$ grows with v_1^t. This growth intensifies viscous dissipation function and consequently more kinetic energy could be dissipated by viscous force. This explains the observation that for the same v_1^n, larger v_1^t results in smaller ε^n.

ACKNOWLEDGMENTS

[1] P. Haines and J. Luers, Aerodynamic penalties of heavy rain on landing airplanes, J. Aircr. **20**, 111 (1983).

[2] B. Derby, Inkjet printing of functional and structural materials: Fluid property requirements, feature stability, and resolution, Annu. Rev. Mater. Res. **40**, 395 (2010).

[3] R. Rioboo, C. Tropea, and M. Marengo, Outcomes from a drop impact on solid surfaces, Atomization Sprays **11**, 12 (2001).

[4] C. Josserand and S. T. Thoroddsen, Drop impact on a solid surface, Annu. Rev. Fluid Mech. **48**, 365 (2016).

[5] D. Richard, C. Clanet, and D. Quéré, Contact time of a bouncing drop, Nature (London) **417**, 811 (2002).

[6] J. C. Bird, R. Dhiman, H.-M. Kwon, and K. K. Varanasi, Reducing the contact time of a bouncing drop, Nature (London) **503**, 385 (2013).

[7] Y. Liu, L. Moevius, X. Xu, T. Qian, J. M. Yeomans, and Z. Wang, Pancake bouncing on superhydrophobic surfaces, Nat. Phys. **10**, 515 (2014).

[8] J. Song, M. Gao, C. Zhao, Y. Lu, L. Huang, X. Liu, C. J. Carmalt, X. Deng, and I. P. Parkin, Large-area fabrication of droplet pancake bouncing surface and control of bouncing state, ACS Nano **11**, 9259 (2017).

[9] A. Mazloomi Moqaddam, S. S. Chikatamarla, and I. V. Karlin, Drops bouncing off macro-textured superhydrophobic surfaces, J. Fluid Mech. **824**, 866 (2017).

[10] A. I. Aria and M. Gharib, Physicochemical characteristics and droplet impact dynamics of superhydrophobic carbon nanotube arrays, Langmuir **30**, 6780 (2014).

[11] D. G. K. Aboud and A.-M. Kietzig, On the oblique impact dynamics of drops on superhydrophobic surfaces. Part II: Restitution coefficient and contact time, Langmuir **34**, 9889 (2018).

[12] Y. H. Yeong, J. Burton, E. Loth, and I. S. Bayer, Drop impact and rebound dynamics on an inclined superhydrophobic surface, Langmuir **30**, 12027 (2014).

[13] D. G. K. Aboud and A.-M. Kietzig, On the oblique impact dynamics of drops on superhydrophobic surfaces. Part I: Sliding length and maximum spreading diameter, Langmuir **34**, 9879 (2018).

[14] C. Antonini, F. Villa, and M. Marengo, Oblique impacts of water drops onto hydrophobic and superhydrophobic surfaces: Outcomes, timing, and rebound maps, Exp. Fluids **55**, 1713 (2014).

[15] D. G. K. Aboud and A.-M. Kietzig, Splashing threshold of oblique droplet impacts on surfaces of various wettability, Langmuir **31**, 10100 (2015).

[16] J. C. Bird, S. S. H. Tsai, and H. A. Stone, Inclined to splash: Triggering and inhibiting a splash with tangential velocity, New J. Phys. **11**, 063017 (2009).

[17] C. Yin, T. Wang, Z. Che, M. Jia, and K. Sun, Oblique impact of droplets on microstructured superhydrophobic surfaces, Int. J. Heat Mass Transfer **123**, 693 (2018).

[18] M. Schremb, I. V. Roisman, and C. Tropea, Transient effects in ice nucleation of a water drop impacting onto a cold substrate, Phys. Rev. E **95**, 022805 (2017).

[19] P. Zhu, C. Chen, K. Nandakumar, and L. Wang, Nonspecular reflection of droplets, Small **17**, 2006695 (2020).

[20] S. O. Unverdi, A front-tracking method for viscous, incompressible, multi-fluid flows, J. Comput. Phys. **100**, 25 (1992).

[21] M. Choi, G. Son, and W. Shim, A level-set method for droplet impact and penetration into a porous medium, Comput. Fluids **145**, 153 (2017).

[22] C. W. Hirt and B. D. Nichols, Volume of fluid (VOF) method for the dynamics of free boundaries, J. Comput. Phys. **39**, 201 (1981).

[23] S. M. Damián, An extended mixture model for the simultaneous treatment of short and long scale interfaces, Ph.D. thesis, National University of Litoral, 2013.

[24] S. S. Deshpande, L. Anumolu, and M. F. Trujillo, Evaluating the performance of the two-phase flow solver InterFoam, Comput. Sci. Discov. **5**, 014016 (2012).

[25] J. U. Brackbill, D. B. Kothe, and C. Zemach, A continuum method for modeling surface tension, J. Comput. Phys. **100**, 335 (1992).

[26] C. Kunkelmann, Numerical modeling and investigation of boiling phenomena, Ph.D. thesis, Technical University of Darmstadt, 2011.

[27] T. Holzmann, *Mathematics, numerics, derivations and Open FOAM(R)*, Release 7.0 (Holzmann CFD, Leoben, 2017), https://Holzmann-cfd.de.

[28] S. F. Kistler, *Hydrodynamics of Wetting* (Marcel Dekker, New York, 1993).

[29] Y. Yao, C. Li, H. Zhang, and R. Yang, Modelling the impact, spreading and freezing of a water droplet on horizontal and inclined superhydrophobic cooled surfaces, Appl. Surf. Sci. **419**, 52 (2017).

[30] A. Russo, M. Icardi, M. Elsharkawy, D. Ceglia, P. Asinari, and C. M. Megaridis, Numerical simulation of droplet impact on wettability-patterned surfaces, Phys. Rev. Fluids **5**, 074002 (2020).

[31] M. Pasandideh-Fard, Y. M. Qiao, S. Chandra, and J. Mostaghimi, Capillary effects during droplet impact on a solid surface, Phys. Fluids **8**, 650 (1996).

[32] C. Clanet, C. Béguin, D. Richard, and D. Quéré, Maximal deformation of an impacting drop, J. Fluid Mech. **517**, 199 (2004).

[33] I. V. Roisman, Inertia dominated drop collisions. II. An analytical solution of the Navier–Stokes equations for a spreading viscous film, Phys. Fluids **21**, 052104 (2009).

[34] C. Ukiwe and D. Y. Kwok, On the maximum spreading diameter of impacting droplets on well-prepared solid surfaces, Langmuir **21**, 666 (2005).

[35] D. Richard and D. Quéré, Bouncing water drops, EPL **50**, 769 (2000).

[36] D. Bartolo, C. Josserand, and D. Bonn, Singular Jets and Bubbles in Drop Impact, Phys. Rev. Lett. **96**, 124501 (2006).

[37] L. Chen, L. Li, Z. Li, and K. Zhang, Submillimeter-sized bubble entrapment and a high-speed jet emission during droplet impact on solid surfaces, Langmuir **33**, 7225 (2017).

[38] B. A. Puthenveettil, V. K. Senthilkumar, and E. J. Hopfinger, Motion of drops on inclined surfaces in the inertial regime, J. Fluid Mech. **726**, 26 (2013).